Solution-Processable Glass LiI-Li_4SnS_4 Superionic Conductors for All-Solid-State Li-Ion Batteries

Kern Ho Park, Dae Yang Oh, Young Eun Choi, Young Jin Nam, Lili Han, Ju-Young Kim, Huolin Xin, Feng Lin, Seung M. Oh, and Yoon Seok Jung**

Conventional lithium-ion batteries (LIBs) have important large-scale energy storage applications, such as electric vehicles and energy storage systems.[1] However, these applications are limited by the safety concerns arising from the flammability of liquid electrolytes used in LIBs.[1,2] As a promising solution to this issue, all-solid-state lithium batteries (ASLBs) with inorganic solid electrolytes (SEs) have attracted considerable attention.[3] Bulk-type ASLBs, in which the composite electrode consists of a particulate mixture of active materials, SEs, and conductive additives, are considered particularly promising because of their high energy density and scalable fabrication.[3a,3b,3d,3e,3g] Sulphide SEs are highly desirable because of their high ionic conductivities (e.g., $Li_{10}GeP_2S_{12}$ (LGPS):[3a] 1.2×10^{-2} S cm^{-1}, $Li_3P_7S_{11}$:[4] 1.7×10^{-2} S cm^{-1}, Li_6PS_5X[5]) and deformability.[3a,3b,3g] The latter enables the fabrication of 2D contacts with active materials by simple cold-pressing.

Most efforts on the development of SEs thus far have placed a strong emphasis on the high ionic conductivity of the SEs.[3a,g,4–6] However, there is a huge discrepancy between the high ionic conductivities of sulphide SEs and the below-par performance of bulk-type ASLBs,[3g,7] which originates from the limited ionic contact between the active materials and SEs.[3a,b,d,g] For example, cold-pressed composite electrodes have exhibited porosities as high as 20%–30%, reflecting poor surface coverage of SEs on the active materials.[7b] Therefore, the fabrication of composite electrodes with more intimate ionic contacts should be a prime objective for future development.[3g,7b,8] However, this development has been inhibited by the drawbacks associated with the conventional protocols of synthesizing sulphide SEs, such as solid-state reactions[3a,5] and mechanochemical methods.[4]

An alternative architecture of SEs for composite electrodes was demonstrated by depositing a SE ($80Li_2S$-$20P_2S_5$) thin film on active materials by pulsed laser deposition.[8,9] In theory, direct SE coatings on active materials can solve the problem of poor ionic contact in bulk-type ASLBs, thus increasing the power and energy densities at the electrode and cell levels.[9,10] However, the vacuum deposition method might be prohibitive for commercialization. In contrast, a scalable solution-based coating method could provide the necessary breakthrough for developing better sulphide SEs and ASLBs. It was reported that Thio-LISICON ($Li_{3.25}Ge_{0.25}P_{0.75}S_4$) showing 1.82×10^{-4} S cm^{-1} can be prepared by using anhydrous hydrazine.[11] However, the use of extremely dangerous anhydrous hydrazine excludes interests for further development. Liang and co-workers reported the synthesis of β-Li_3PS_4 with an ionic conductivity of 1.6×10^{-4} S cm^{-1} by using tetrahydrofuran[12] and $Li_7P_2S_8I$ with an ionic conductivity of 6.3×10^{-4} S cm^{-1} by using acetonitrile.[13] In both cases, however, the solutions are neither homogeneous nor environmentally friendly. The Tatsumisago group reported that N-methylformamide (b.p. = 182.6 °C) can dissolve Li_3PS_4 (LPS) to form a homogenous solution, and LPS with a conductivity of 2.6×10^{-6} S cm^{-1} can be recrystallized.[14] The same group later showed that argyrodite Li_6PS_5Cl with an ionic conductivity of 1.4×10^{-5} S cm^{-1} can be prepared by using ethanol.[15] It is also worth mentioning that Li_4SnS_4 with an ionic conductivity of 7×10^{-5} S cm^{-1} was prepared at 320 °C from aqueous solution, where water was used to obtain a high-purity crystalline phase.[16] A major challenge in developing solution-processable sulphide SEs is the simultaneous fulfillment of all the following requirements: forming a homogeneous solution for the coatable process, using nontoxic and safe solvents with low boiling points, and ensuring sufficiently high ionic conductivities (>10^{-4} S cm^{-1}). Another critical issue regarding sulphide SEs is their instability in air.[17] As-substituted Li_4SnS_4 exhibiting stability in air and high conductivity (1.39×10^{-3} S cm^{-1}) was recently prepared by a solid-state reaction at 450 °C.[18] However, the application of this SE may

K. H. Park, D. Y. Oh, Y. E. Choi, Y. J. Nam, Prof. Y. S. Jung
School of Energy and Chemical Engineering
Department of Energy Engineering
Ulsan National Institute of Science and Technology (UNIST)
Ulsan 689-798, South Korea
E-mail: ysjung@unist.ac.kr
K. H. Park, Prof. S. M. Oh
School of Chemical and Biological Engineering
Seoul National University
599 Gwanangno
Gwanak-gu, Seoul 151-742, South Korea
E-mail: seungoh@snu.ac.kr
L. Han, Dr. H. Xin
Center for Functional Nanomaterials
Brookhaven National Laboratory
Upton, NY 11973, USA
Prof. J.-Y. Kim
Materials Science and Engineering
Ulsan National Institute of Science and Technology (UNIST)
Ulsan 689-798, South Korea
Dr. F. Lin
Energy Storage and Distributed Resources Division
Lawrence Berkeley National Laboratory
Berkeley, CA 94720, USA

DOI: 10.1002/adma.201505008

be hindered owing to the use of arsenic, which is extremely toxic.

Here, we report the development of a new class of solution-coatable superionic conductor, LiI-Li_4SnS_4, which enables us to achieve direct ionic contacts on active materials with highly conductive solidified electrolyte coating. Glass 0.4LiI-0.6Li_4SnS_4 is prepared at 200 °C from a homogenous MeOH solution to exhibit high ionic conductivity (4.1×10^{-4} S cm^{-1} at 30 °C), excellent deformability, and dry-air-stability. The conductivity of 4.1×10^{-4} S cm^{-1} is the highest among all inorganic SEs prepared from homogeneous solution. We find that the deformability and ionic conductivity of the solution-processed Li_4SnS_4 are significantly enhanced at lower preparation temperature and by the addition of LiI. Importantly, the solution-processed 15 wt% 0.4LiI-0.6Li_4SnS_4 coating on $LiCoO_2$ ensures much higher surface coverage on $LiCoO_2$ (81%) than that for conventional mixture electrodes (31%), thus allowing a significant enhancement of the rate capabilities. Our results represent the first demonstration of the high potential of ASLBs fabricated by a scalable and coatable solution process.

For the synthesis of xLiI-(1-x)Li_4SnS_4 ($0.0 \le x \le 0.5$), solutions were prepared by dissolving both LiI and Li_4SnS_4 together into anhydrous MeOH. **Figure 1**a shows the homogenous MeOH solution containing fully dissolved LiI and Li_4SnS_4 (0.46 M of a formula unit of 0.4LiI-0.6Li_4SnS_4, 100 mg mL^{-1}). Powders obtained by drying the as-prepared solution under vacuum at room temperature were subjected to thermogravimetric analysis (TGA) under N_2, as shown in Figure 1b. Owing to its low boiling point (64.7 °C), MeOH was removed below 160 °C, based on which three different heat-treatment (HT) temperatures (200, 320, and 450 °C) were selected. Hereafter, xLiI-(1-x)Li_4SnS_4 prepared at a temperature of y (°C) is referred to as "xLiI-(1-x)LSS-y".

Figure 1c,d shows the X-ray diffraction (XRD) patterns and ionic conductivities at 30 °C with activation energies for xLiI-(1-x)Li_4SnS_4 samples ($0.0 \le x \le 0.5$) prepared at different temperatures. The sample prepared at 450 °C exhibits a pure crystalline Li_4SnS_4.[16] As the HT temperature is decreased to 320 °C, the XRD pattern shows lowered crystallinity. Decreasing the HT temperature further to 200 °C results in an almost amorphous feature. The ionic conductivities of cold-pressed pellets prepared under 370 MPa were measured using Li-ion blocking c-Al/SE/c-Al cells (c-Al: carbon-coated Al foil) by the AC impedance method (Nyquist and Arrhenius plots are shown in Figure S1, Supporting Information). Li_4SnS_4 prepared at 450 °C exhibits a conductivity of 1.0×10^{-5} S cm^{-1}. Surprisingly, decreasing the HT temperature leads to an increase in the conductivity (2.1×10^{-5} S cm^{-1} at 320 °C and 8.9×10^{-5} S cm^{-1} at 200 °C). Considering that a minimum temperature of 320 °C is required for complete dehydration when using an aqueous solution,[16] the significantly enhanced conductivity at 200 °C in this work highlights the exceptional benefit of using the low-boiling-point MeOH. As x in x LiI-(1-x)Li_4SnS_4 increases up to 0.4, the XRD-amorphous features are retained and the conductivity increases gradually, with the highest conductivity value reaching 4.1×10^{-4} S cm^{-1} and the lowest activation energy reaching 41.6 kJ mol^{-1}. Subsequently, the conductivity is decreased at $x = 0.5$, at which the segregated crystalline LiI (JCPDS No. 71–3746) is observed (Figure 1c). Apart from one exception ($x = 0.0$ vs 0.1), the activation energies inversely follow the trend of ionic conductivities. Consistent with the results from the AC impedance method, the activation energy obtained from motional narrowing of the ^{7}Li nuclear magnetic resonance (NMR) data[19] also confirms the lower activation energy of 0.4LiI-0.6LSS-200 (24.7 kJ mol^{-1}) compared to that of LSS-200 (27.3 kJ mol^{-1}) (see the Supporting Information for details, Figure S2). The difference in the activation energy values from the AC impedance and the ^{7}Li NMR stems from the different time windows of sensing.[20] While NMR is sensitive to local Li-ion hopping, AC impedance is sensitive to the overall contributions of Li-ion movements, such as grain boundary resistance. Increasing HT temperature for 0.4LiI-0.6Li_4SnS_4 to 450 °C resulted in the formation of SnI_4 and a decrease in conductivity (4.0×10^{-6} S cm^{-1}, Figure S3, Supporting Information). Overall, it is evident that both the composition (the inclusion of LiI) and the structure (whether XRD-amorphous or crystalline as well as whether crystalline LiI is segregated or not) affect the ionic conductivities.

As the first step to elucidate the microstructures of LiI-Li_4SnS_4, high-resolution transmission electron microscopy (HRTEM) analyses were carried out. Figure 1e,f exhibits HRTEM images and their corresponding selected-area electron diffraction (SAED) patterns for LSS-200 and 0.4LiI-0.6LSS-200, respectively. Contrary to the XRD-amorphous feature in Figure 1c, the LSS-200 here appears to consist of nanometer-sized crystallites. The lattice fringes and the SAED patterns in the inset of Figure 1e unequivocally indicates that the nanocrystallites belong to orthorhombic Li_4SnS_4.[16] In sharp contrast, the HRTEM image and the featureless SAED pattern in Figure 1f reveal a completely amorphous structure for 0.4LiI-0.6LSS-200, indicating that the added LiI acts as the glass former by dissolving into Li_4SnS_4. The aberration-corrected scanning TEM (STEM) image and its corresponding energy dispersive X-ray spectroscopy (EDXS) elemental maps of Sn, S, and I for 0.4LiI-0.6LSS-200 in Figure S4 of the Supporting Information show homogeneous composition all over the particle. The homogeneous distribution of Li is also confirmed by the STEM image and its corresponding electron energy loss spectroscopy (EELS) map in Figure S5 of the Supporting Information. The Raman spectra for LSS-450, LSS-200, and 0.4LiI-0.6LSS-200 (Figure 1g) show the strong peaks centered at 345 cm^{-1} originating from SnS_4^{4-}.[21] This result implies that the SnS_4^{4-} polyanion is intact regardless of the HT temperature and the inclusion of LiI, which is also corroborated by the similar ^{119}Sn magic angle spinning (MAS) NMR signatures centered at ≈59 ppm for LSS-200 and 0.4LiI-0.6LSS-200 (Figure S6, Supporting Information).[16] Further, Sn K-edge extended X-ray absorption fine structure (EXAFS) spectra for LSS-450, LSS-200, 0.1LiI-0.9LSS-200, 0.3LiI-0.7LSS-200, and 0.4LiI-0.6LSS-200 exhibit the main peaks at an identical radial distance that are attributed to Sn-S bonds from SnS_4^{4-} (Figure S7, Supporting Information). X-ray absorption near edge structure (XANES) spectra for Sn K-edge and I L-edge show no noticeable difference among the samples (Figure S8, Supporting Information). However, a subtle difference between LSS-200 and 0.4LiI-0.6LSS-200 is observed in the ^{119}Sn NMR signatures (Figure S6, Supporting Information), where the 0.4LiI-0.6LSS-200 exhibits a slight negative shift in the peak

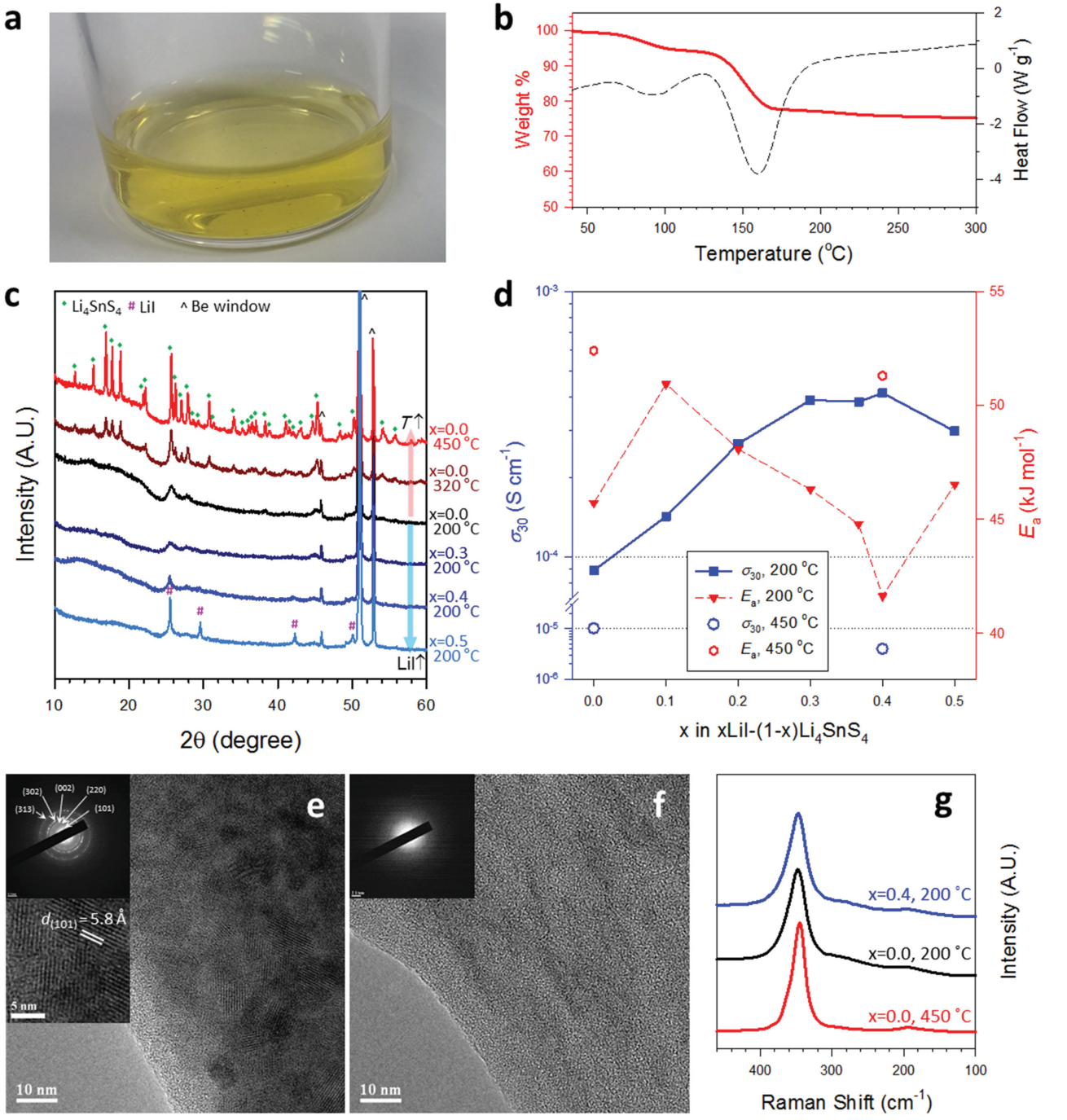

Figure 1. Preparation and characterization of solution-processable *x*LiI-(1-*x*)Li_4SnS_4. a) Photograph of LiI- and Li_4SnS_4-dissolved MeOH. b) TGA profile under N_2 for the powders obtained by drying the solution a under vacuum at room temperature. c) XRD patterns of *x*LiI-(1.0-*x*)Li_4SnS_4. The preparation temperatures are given. d) Conductivities of *x*LiI-(1.0-*x*)Li_4SnS_4 at 30 °C and activation energies as a function of *x* in *x*LiI-(1-*x*)Li_4SnS_4. HRTEM images of e) Li_4SnS_4 and f) 0.4LiI-0.6Li_4SnS_4 prepared at 200 °C. The SAED patterns are provided in the insets. g) Raman spectra for LSS-450, LSS-200, and 0.4LiI-0.6LSS-200.

at 59 ppm as compared to LSS-200, indicating the influence of iodide ions in the proximity of SnS_4^{4-}. From the combined spectroscopic analyses, the microstructure of the solution-processed LiI-Li_4SnS_4 prepared at 200 °C is considered to be a disordered matrix consisting of SnS_4^{4-} and I^- anions around which Li^+ cations occupy the interstitial sites.

Several factors can be considered to account for the enhancement in conductivity after adding LiI to Li_4SnS_4 (0.4LiI-0.6LSS-200: 4.1×10^{-4} S cm^{-1} vs LSS-200: 8.9×10^{-5} S cm^{-1}). As a naïve consideration, the concentration of Li may be related to the conductivity.[22] However, the change in the concentration of Li from Li_4SnS_4 to *x*LiI-(1-*x*)Li_4SnS_4 is marginal (45.2 atomic%

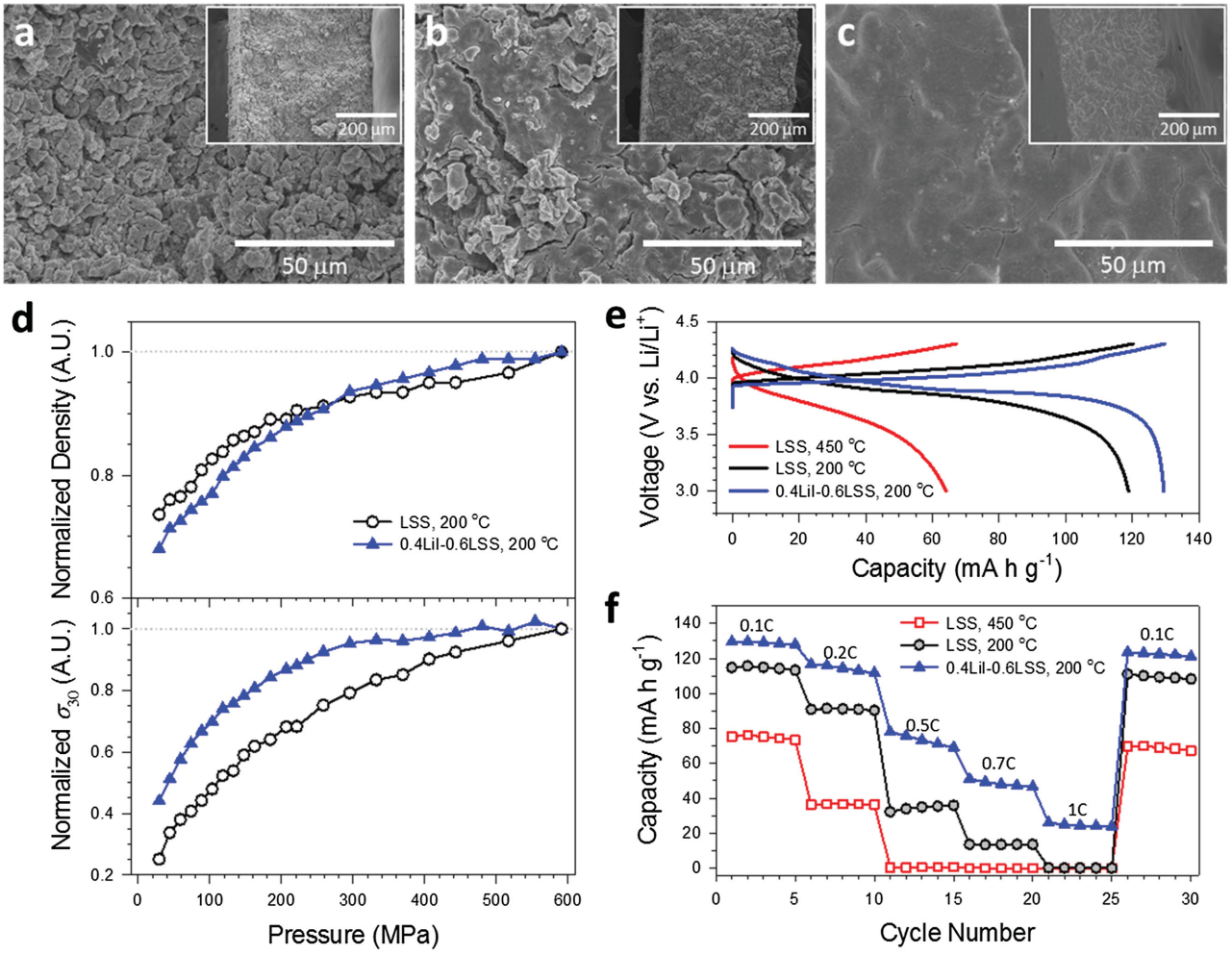

Figure 2. Comparison of deformability of xLiI-(1-x)Li_4SnS_4 and electrochemical performances for $LiCoO_2$/Li-In cells. Fracture cross-sectional FESEM images of a) LSS-450, b) LSS-200, and c) 0.4LiI-0.6LSS-200. d) Normalized densities and conductivities at 30 °C for LSS-200 and 0.4LiI-0.6LSS-200 as a function of pressure. e) Voltage profiles at 0.1C (0.11 mA cm^{-2}) and f) rate capabilities for $LiCoO_2$/Li-In cells in which the electrodes were prepared by mixing $LiCoO_2$ with LSS-450, LSS-200, and 0.4LiI-0.6LSS-200 with a $LiCoO_2$:SE weight ratio of 70:30.

for $x = 0.4$ vs 44.4 atomic% for $x = 0.0$). The increased conductivities at higher x in xLiI-(1-x)Li_4SnS_4 can be explained by highly open frameworks owing to the large ionic radii of iodide ions (0.206 nm)[23] and/or the lower energy barriers for Li-hopping due to the highly polarizable nature of iodide ions,[22,24] which is supported by the fact that the activation energy decreases as x increases from 0.1 to 0.4 (Figure 1d). The decrease in conductivity by replacing the iodide ion by a smaller and less polarizable bromide ion (0.4LiBr-0.6Li_4SnS_4, $r = 0.182$ nm, 1.4×10^{-4} S cm^{-1}) is also in line with the aforementioned explanation. We also need to explain why the nanocrystalline Li_4SnS_4 prepared at 200 °C exhibits much higher conductivity (8.9×10^{-5} S cm^{-1}) than the highly crystalline one prepared at 450 °C (1.0×10^{-5} S cm^{-1}). Apart from bulk conductivity, the deformability of SEs could also account for the measured conductivity since it influences the grain boundary or interfacial contact resistances.[4b]

Figures 2a–c shows fracture cross-sectional images of the cold-pressed pellets of LSS-450 and LSS-200, and 0.4LiI-0.6LSS-200, respectively. For the highly crystalline LSS-450 pellet (Figure 2a), the particles are not deformed/merged well. Decreasing the HT temperature to 200 °C (LSS-200) results in a smoothened cross-sectional surface (Figure 2b), indicating enhanced deformability. Therefore, the main source for the lower conductivity of LSS-450 compared to that of LSS-200 is considered to be the poor interfacial contacts between the particles and grains. The low bond energy at the interfaces between nanocrystallites and/or the defect-rich nanostructures could be responsible for the superior deformation of nanocrystalline Li_4SnS_4 (LSS-200) compared to the highly crystalline one (LSS-450).[8,25] More importantly, for 0.4LiI-0.6LSS-200, an almost poreless fracture cross-sectional surface is observed (Figure 2c). The excellent deformability of 0.4LiI-0.6LSS-200 can be explained by its completely amorphous structure and the presence of iodide ions. Following Fajans' rule, the large size and the high polarizability of iodide ions lead to more covalent nature, resulting in the enhanced deformability.[8,23] The better deformability of 0.4LiI-0.6LSS-200 compared to that of LSS-200 is also confirmed by measurements of density and conductivity

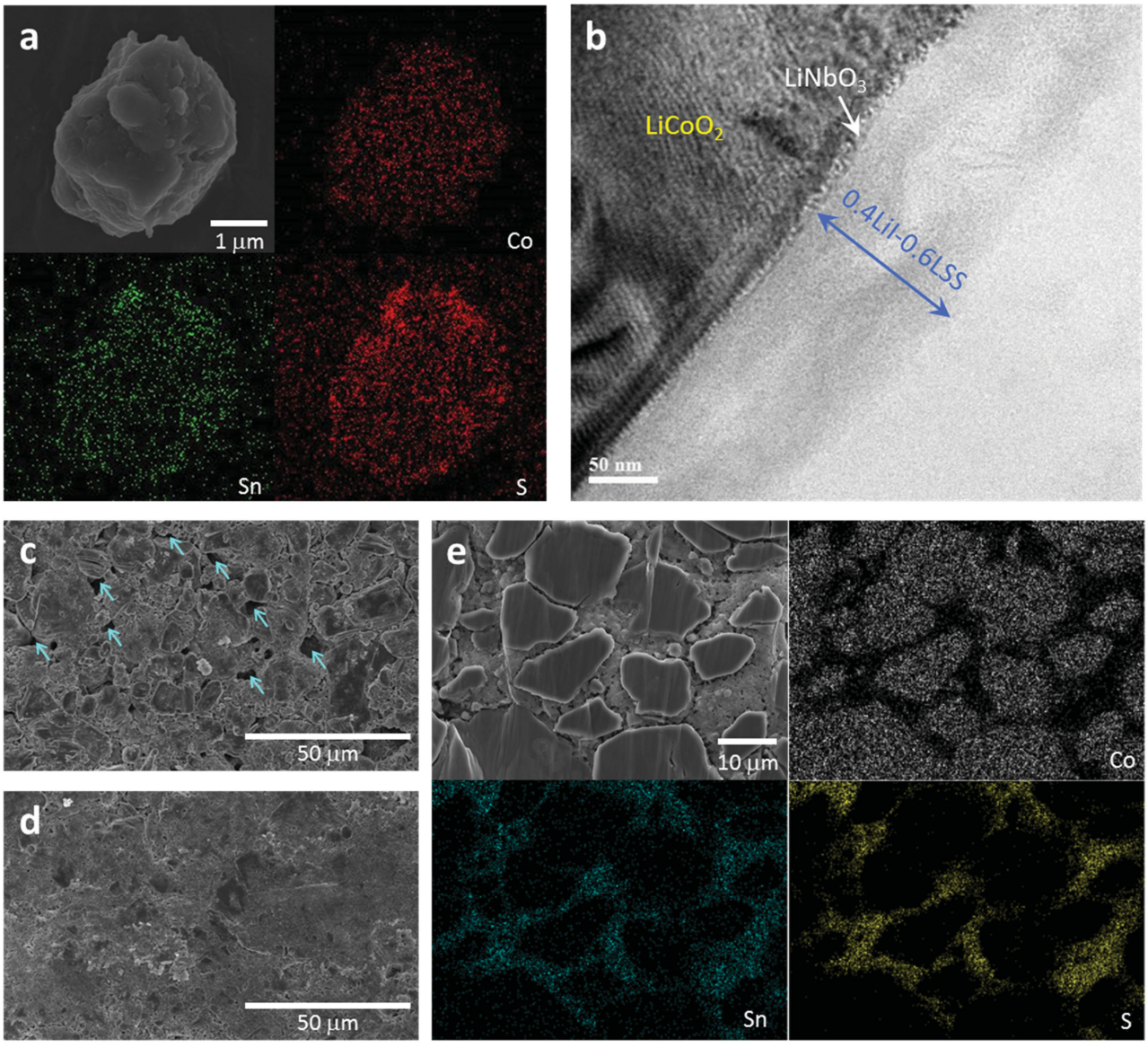

Figure 3. 0.4LiI-0.6Li_4SnS_4-coated $LiCoO_2$. a) FESEM image of 0.4LiI-0.6Li_4SnS_4-coated $LiCoO_2$ particle and its corresponding EDXS elemental maps. b) HRTEM image of FIB-cross-sectioned 0.4LiI-0.6Li_4SnS_4-coated $LiCoO_2$ particle. FESEM surface images of c) 0.4LiI-0.6Li_4SnS_4/$LiCoO_2$ mixture electrode and d) 0.4LiI-0.6Li_4SnS_4-coated $LiCoO_2$ electrode. The arrows indicate void spaces. e) Cross-sectional FESEM image of 0.4LiI-0.6Li_4SnS_4-coated $LiCoO_2$ electrode and the corresponding EDXS elemental maps. The $LiCoO_2$:SE weight ratio was 85:15.

as a function of applied pressure. As shown in Figure 2d, the density and the conductivity are saturated at far lower pressures for 0.4LiI-0.6LSS-200 than for LSS200. When the electrodes are prepared by mixing $LiCoO_2$ with 30 wt% of these SEs and assembled as $LiCoO_2$/Li-In cells, the variations in the electrochemical performances appear dramatic. Figure 2e,f shows the voltage profiles at 0.11 mA cm^{-2} (0.1C) and the associated rate capabilities, respectively. The better performances of the lower overpotential and the higher capacity are achieved for the SEs in the order of 0.4LiI-0.6LSS-200, LSS-200, and LSS-450, thus highlighting the importance of both ionic conductivity and deformability. The excellent deformability of LiI-Li_4SnS_4 would also be advantageous for buffering the volume change of active materials upon repeated charge and discharge.[8] Further exploration on incorporation of other highly polarizable elements and alio-/iso-valent substitutions for Sn and S of Li_4SnS_4 along with fine control of microstructure by solution-process may open opportunities to achieve higher conductivities (>10^{-3} S cm^{-1}) than that for 0.4LiI-0.6Li_4SnS_4.

0.4LiI-0.6Li_4SnS_4-coated $LiCoO_2$ powders were obtained from the LiI- and Li_4SnS_4-dissolved MeOH solution in the presence of $LiCoO_2$ particles. Since the SE precursor solution wets any exposed surfaces (even porous surfaces) of the $LiCoO_2$ particles and is solidified, it is possible to achieve direct ionic contacts comparable to those in the case of conventional LIBs using liquid electrolytes. **Figure 3**a shows an field-emission scanning electron microscopy (FESEM) image of the coated $LiCoO_2$ particle and its corresponding EDXS elemental maps,

which confirm uniform SE coatings and their homogeneous composition. (The EDXS elemental map for iodine is shown in Figure S9, Supporting Information.) Direct visualization of the SE coating layer was achieved by HRTEM using a focused ion beam (FIB) cross-sectioned sample as seen in Figure 3b. An amorphous SE layer of approximately 100 nm thickness covers the $LiCoO_2$, which is also corroborated by an annular dark field (ADF) STEM image and its corresponding EDXS elemental maps (Figure S10, Supporting Information). The direct coating of SEs on active materials offers significant advantages over the conventional mixture electrodes, such as intimate ionic contacts and better spatial distribution of SEs. Figure 3c,d shows FESEM images of the surface of the $LiCoO_2$ composite electrodes prepared by cold-pressing a mixture of $LiCoO_2$ and $0.4LiI\text{-}0.6Li_4SnS_4$ powders and that of the $0.4LiI\text{-}0.6Li_4SnS_4$-coated $LiCoO_2$ electrode. While voids are seen between particles in the mixture electrode, the SE-coated $LiCoO_2$ electrode exhibits a smooth and flat surface. Upon cold-pressing, the soft SEs are deformed by the hard $LiCoO_2$ particles and are squeezed to fill the voids between the $LiCoO_2$ particles. The voids observed in the mixture electrode (Figure 3c) reflect poor spatial distribution of SEs and their limited contacts with $LiCoO_2$ particles (Figure 3d). In sharp contrast, a cross-sectioned FESEM and the corresponding EDXS elemental maps for the SE-coated $LiCoO_2$ electrode in Figure 3e show that the SEs are well distributed by filling the spaces between the $LiCoO_2$ particles without noticeable voids, thus implying excellent ionic conduction pathways. (The EDXS elemental map for iodine is shown in Figure S11, Supporting Information.) This is also consistent with much lower porosity for the $0.4LiI\text{-}Li_4SnS_4$-coated $LiCoO_2$ electrode (7%) than that for the conventional mixture electrode (12%) (see the Supporting Information for details).

The advantage in ionic contacts by SE coatings on active materials is evaluated by comparing the electrochemical performances of $LiCoO_2$/Li-In cells made of the $0.4LiI\text{-}0.6Li_4SnS_4$-coated $LiCoO_2$ electrode with the ones made of the conventional mixture electrode (**Figure 4**). The weight fraction of SE was 15 wt%. A diagnostic electrochemical analysis was first carried out by comparing the electrochemical impedance spectroscopy (EIS) responses for $LiCoO_2$/LPS/Li-In cells (configuration is depicted in Figure S12a, Supporting Information). The Nyquist plots in Figure 4a show one semicircle followed by the Warburg tail. The intercept values at the *x*-axis and the size of the semicircle are assigned as the resistance of LPS SE layer (≈54 Ω) and the interfacial resistance, respectively.[10] The semicircle for SE-coated $LiCoO_2$ electrode (≈16 Ω) is smaller than half that of the mixture electrode (≈39 Ω), which can be explained by its much superior ionic contacts. Figure 4b compares the discharge capacities varied by the current densities for $LiCoO_2$/LPS/Li-In cells. Consistent with the EIS results in Figure 4a, a pronounced improvement in the rate capability for the SE-coated $LiCoO_2$ electrode over the mixture electrode is observed. The performance of the mixture electrode is affected by mixing conditions. The mixture electrode obtained using a vortex mixer shows even inferior performance compared to the manually mixed electrode. This result indicates that the use of SE-coated active materials can lessen the need of process control for mixing during electrode fabrication. Considering the higher conductivity of LPS (1.0×10^{-3} S cm^{-1}) than that of 0.4LiI-0.6LSS-200 (4.1×10^{-4} S cm^{-1}), the poor performance of the $LiCoO_2$/LPS mixture electrode (open square) implies the importance of ionic contacts (and deformability) over conductivity on the overall performance of bulk-type ASLBs. When the LPS/LGPS bilayer having lower resistance (≈13 Ω, LGPS: 6.0×10^{-3} S cm^{-1}) replaces the LPS SE layer (≈54 Ω) (configuration is depicted in Figure S12b, Supporting Information), a more dramatic improvement of the SE-coated $LiCoO_2$ electrode over the mixture electrode is achieved (Figure 4c). The SE-coated $LiCoO_2$ electrode shows the capacity retention of 83.3% at 1C (113 mA h g^{-1}) as compared to the capacity at 0.1C (135 mA h g^{-1}) while the mixture electrode shows only 46.0% (60 mA h g^{-1}). In the discharge voltage profiles for the $LiCoO_2$/(LPS/LGPS)/Li-In cells in Figure 4d, the SE-coated $LiCoO_2$ electrode shows a much lower polarization and the resulting higher capacities compared to the mixture electrode. Moreover, the 0.4LiI-0.6LSS-coated $LiCoO_2$ electrode also outperforms the $LiCoO_2$/LGPS mixture electrode (Figure 4c, and Figure S13, Supporting Information). This result is surprising in that the conductivity of LGPS (6.0×10^{-3} S cm^{-1}) is more than one order of magnitude higher than that for 0.4LiI-0.6LSS (4.1×10^{-4} S cm^{-1}), which again highlights the decisive role of intimate ionic contacts over ionic conductivity on the overall performance of bulk-type ASLBs. Further optimization of the rate performance would be possible by a combination of 0.4LiI-0.6LSS-coated $LiCoO_2$ and LGPS powders, which can synergize the intimate ionic contacts by the 0.4LiI-0.6LSS coating and the extremely fast ionic transport through the LGPS. This strategy will be our next mission. As shown in the inset in Figure 4c, the 0.4LiI-0.6LSS-coated $LiCoO_2$ electrode cycled at 1C also exhibits the excellent cycleability (capacity retention of 95.7% after 80 cycles).

Finally, the galvanostatic intermittent titration technique (GITT) was employed to track the polarization.[26] Transient voltage profiles and polarization curves for $LiCoO_2$/LPS/Li-In cells are plotted in Figure 4e. The whole range shows a higher polarization for the mixture electrode than that for the SE-coated $LiCoO_2$ electrode. Moreover, the interfacial contact areas between $LiCoO_2$ and the SEs were extracted by analyzing the transient voltage profiles (Figure 4e, and Figure S14) (see the Supporting Information for details).[27] Notably, the surface coverage of SEs over the $LiCoO_2$ in the SE-coated $LiCoO_2$ electrode (81%) turns out to be 2.6 times higher than that in the mixture electrode (31%). Figure 4f shows schematic diagrams illustrating the uneven spatial distribution of SEs and the poor ionic contacts in the mixture electrode as compared to the SE-coated $LiCoO_2$ electrode, which is confirmed by the surface images of electrodes (Figure 3c,d) and the porosity values (7% for the SE-coated $LiCoO_2$ electrode and 12% for the mixture electrode). These features are responsible for the resulting electrochemical behaviors shown in Figure 4a–e. The improved performance by solution-processed coating on active materials was also demonstrated for Li_4SnS_4-coated $Li_4Ti_5O_{12}$ as the anode material (Figure S15, Supporting Information). A 2.7 wt% coating of Li_4SnS_4 on $Li_4Ti_5O_{12}$ resulted in increase in the reversible capacity at 0.2C from 90 to 140 mA h g^{-1}. Overall, all the electrochemical results unequivocally demonstrate the superiority of the electrode fabricated from the SE-coated active

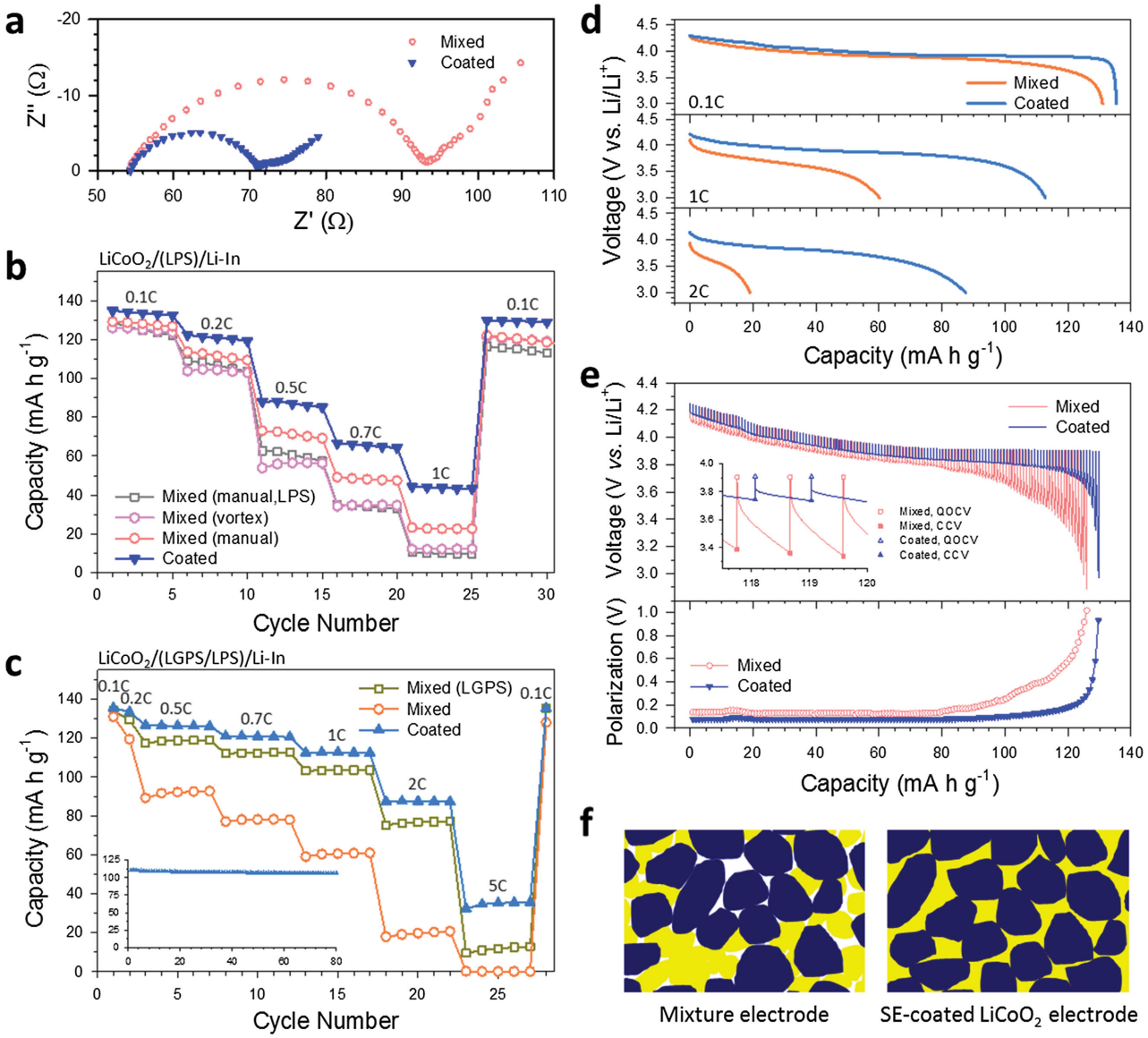

Figure 4. Comparative electrochemical characterization of mixture electrode and 0.4LiI-0.6Li_4SnS_4-coated $LiCoO_2$ electrode. a) Nyquist plots for $LiCoO_2$/LPS/Li-In cells. Rate capabilities of $LiCoO_2$/SE/Li-In cells when the SE layer is b) Li_3PS_4 (LPS) (Figure S12a,c, Supporting Information) LGPS/LPS bilayer (Figure S12b, Supporting Information). Two mixture electrodes, one prepared by manual mixing and one using a vortex mixer, are compared in (b). The results of (b) the LPS/$LiCoO_2$ and c) the LGPS/$LiCoO_2$ mixture electrode are also shown for comparison. Cycle performance at 1C for the 0.4LiI-0.6LSS-coated $LiCoO_2$ electrode is shown in the inset in (c). d) Discharge voltage profiles for $LiCoO_2$/(LGPS/LPS)/Li-In cell. e) Transient discharge voltage profiles and their corresponding polarization plots obtained by GITT for $LiCoO_2$/LPS/Li-In cell. The enlarged view is shown in the inset. The polarization curves were plotted by subtracting CCV from QOCV in the transient voltage profiles. The $LiCoO_2$:SE weight ratio was 85:15. f) Schematic illustration of the mixture electrode and the 0.4LiI-0.6Li_4SnS_4-coated $LiCoO_2$ electrode. The dark blue and yellow regions indicate $LiCoO_2$ and SE, respectively.

materials over the mixture electrode, thus revealing the importance of intimate ionic contacts in bulk-type ASLBs. Practical bulk-type ASLBs would require the inclusion of organic components, such as polymeric binders[28] and nonwoven scaffolds,[10] that provide flexibility and/or better adhesion. However, ionic blockage by those organic components would result in a significant trade-off in the rate performance. The direct ionic contact between active materials and highly conductive 0.4LiI-0.6Li_4SnS_4 is thus expected to considerably affect the performance of practical bulk-type ASLBs.

Finally, the dry-air-stability of 0.4LiI-0.6Li_4SnS_4 was tested. The conductivity after exposing the 0.4LiI-0.6Li_4SnS_4 powders to dry air for 24 h at 30 °C was still high (from 4.1×10^{-4} S cm^{-1} to 2.6×10^{-4} S cm^{-1}). This is in sharp contrast to the LPS powders, whose conductivity decreased by more than two orders of magnitude (from 1.0×10^{-3} to 8.0×10^{-6} S cm^{-1}) (Figure S16, Supporting Information). The changes in the electrochemical performances of $LiCoO_2$/LPS/Li-In cells fabricated from the LPS/$LiCoO_2$ mixture electrodes and the 0.4LiI-0.6Li_4SnS_4-coated $LiCoO_2$ electrodes before and after exposure to dry air for

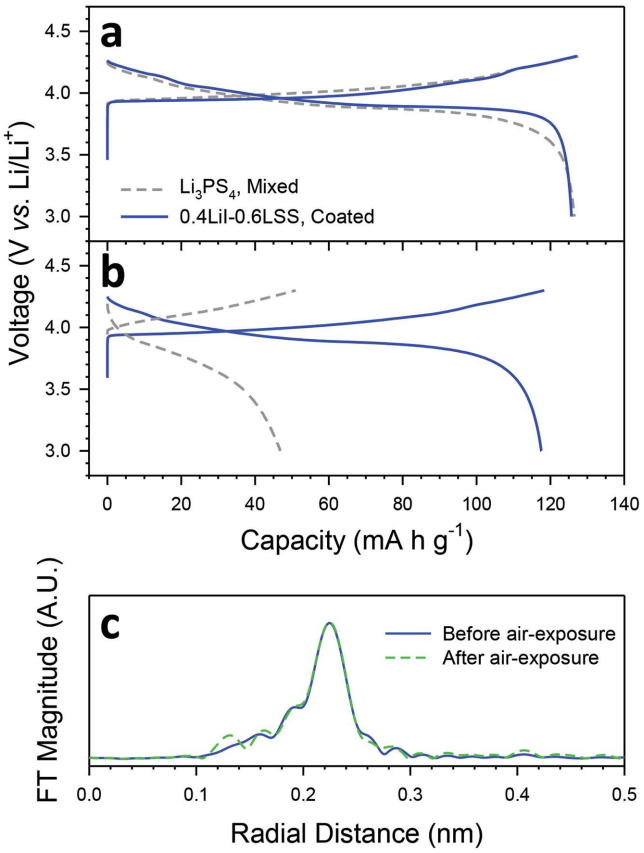

Figure 5. Dry-air-stability of 0.4LiI-0.6Li_4SnS_4. Voltage profiles of $LiCoO_2$/LPS/Li-In cells in which the $LiCoO_2$ composite electrodes are the LPS/$LiCoO_2$ mixture electrode or the 0.4LiI-0.6Li_4SnS_4-coated $LiCoO_2$ electrode a) before and b) after exposure of the LPS powders and the 0.4LiI-0.6Li_4SnS_4-coated $LiCoO_2$ powders to dry air for 24 h. The C-rate was 0.1C (0.11 mA cm^{-2}). c) Sn K-edge EXAFS spectra for 0.4LiI-0.6Li_4SnS_4-coated $LiCoO_2$ powders before and after exposure to dry air. The $LiCoO_2$:SE weight ratio was 85:15.

24 h at 30 °C are also compared. When cycled at 0.11 mA cm^{-2} (0.1C), after exposure to dry air, the 0.4LiI-0.6Li_4SnS_4-coated $LiCoO_2$ electrode shows negligible decrease in capacity, whereas the LPS/$LiCoO_2$ mixture electrode exhibits significantly increased polarization and decreased capacity (**Figures 5**a,b), indicating that the solution-processable LiI-Li_4SnS_4 has potential compatibility with practical applications.[29] The inertness of 0.4LiI-0.6Li_4SnS_4 against dry air is confirmed by the negligible change in the Sn K-edge EXAFS signature (Figure 5c). The excellent stability of 0.4LiI-0.6Li_4SnS_4 is in line with the results of previous works for As-substituted Li_4SnS_4[18] and Li_2SnS_3,[30] and is explained by adopting the hard and soft acid and base (HSAB) theory.[7b,18] The soft acid, Sn, is less vulnerable toward attack by the hard base, O, than the hard acid, P.

Similar to the case of LGPS, one drawback of Li_4SnS_4-based SEs is their poor reduction stability at <1 V (vs Li/Li^+) because Sn acts as a reducing centre.[31] However, it does not neutralize the promising advantages of LiI-Li_4SnS_4. In contrast to conventional LIBs using a single liquid electrolyte, configuring with more than one SE is a significant benefit for ASLBs. For example, $3LiBH_4 \cdot$LiI-coated As-substituted Li_4SnS_4 is operable with Li metal,[18] and TiS_2/(LGPS/LPS)/Li-In cell maximizes the rate capability with retaining reversibility.[10,31b] The latter is also the case for the results of (0.4LiI-0.6LSS-coated $LiCoO_2$)/(LGPS/LPS)/Li-In cell shown in Figure 4c,d, and Figure S12b of the Supporting Information.

In summary, we successfully demonstrated the application of a new, highly conductive, highly deformable, and dry-air-stable glass 0.4LiI-0.6Li_4SnS_4 prepared at 200 °C from a homogeneous MeOH solution for the scalable solution coating with intimate ionic contacts. The combined spectroscopic and electrochemical analyses revealed the importance of the microstructure and the inclusion of LiI on the properties of SEs (conductivity and deformability). Importantly, the comprehensive electron microscopy and electrochemical analyses revealed the significant impact of intimate ionic contacts between the active materials and SEs for the 0.4LiI-0.6Li_4SnS_4-coated $LiCoO_2$ electrodes, as compared to the conventional mixture electrodes. The excellent capacity retention of the 0.4LiI-0.6Li_4SnS_4-coated $LiCoO_2$ electrode upon exposure to dry air is also very promising for ASLB applications. It should be emphasized that this solution-processable LiI-Li_4SnS_4 unprecedentedly satisfies both high performance and high potential for practical applications. We believe that our results provide new insight into the design/synthesis of ionic conductors as well as a breakthrough for the scalable fabrication of practical all-solid-state batteries.

Experimental Section

Preparation of Materials: Crystalline Li_4SnS_4 powders as precursors for the solution process were prepared by heat-treatment of 2 g of a pelletized stoichiometric mixture of Li_2S (99.9%, Alfa Aesar) and SnS_2 (99.999%, American elements) at 450 °C in a quartz ampoule sealed under vacuum. For the solution-based synthesis of LiI-Li_4SnS_4, a stoichiometric amount of the as-prepared Li_4SnS_4 and LiI (99.95%, Alfa Aesar) was dissolved into anhydrous MeOH (99.8%, Sigma-Aldrich) under dry Ar. For typical preparation, 0.36–0.49 M solution (concentration for xLiI-(1-x)Li_4SnS_4 or 100 mg (mL of MeOH)$^{-1}$) was used. After the powders were obtained under vacuum at room temperature, further heat-treatment under vacuum at designated temperatures (200, 320, and 450 °C) resulted in the final samples. The solution-processable LiBr-Li_4SnS_4 powders were prepared by using LiBr (99.95%, Alfa Aesar) and Li_4SnS_4 by following the same procedure as that for LiI-Li_4SnS_4. The 0.4LiI-0.6Li_4SnS_4-coated $LiCoO_2$ powder was prepared by the same solution process in the presence of $LiCoO_2$ powders with a HT temperature of 200 °C; In order to mitigate undesirable side reactions, 0.3 wt% $LiNbO_3$-coated $LiCoO_2$ powders were used.[3a,g,32] The entire preparation procedure was carried out without exposure to air. The LPS (1.0×10^{-3} S cm^{-1} at 30 °C) and LGPS (6.0×10^{-3} S cm^{-1} at 30 °C) powders were prepared by ball-milling followed by HT at 243 °C for 1 h and by solid-state reaction at 550 °C, respectively, as described in our previous reports.[7b,10]

Materials Characterization: The TGA profile was obtained from 25 to 600 °C at 0.167 °C s^{-1} under N_2 using a SDT Q600 (TA Instrument Corp.). XRD cells containing hermetically sealed LiI-Li_4SnS_4 samples with a beryllium window were mounted on a D8-Bruker Advance diffractometer equipped with Cu K_α radiation (0.154056 nm), and were subjected to measurements at 40 kV and 40 mA using a continuous scanning mode at 0.025° s^{-1}. The Raman spectra were measured using a Raman spectrometer (Alpha300R, WITec) with a 532 nm He–Ne laser. The HRTEM and EDXS elemental mapping images were obtained using JEM-2100F (JEOL). The HRTEM images were obtained with 200 kV of acceleration voltage. The EDXS elemental mapping

images were obtained using 80 mm^2 X-Max silicon drift detector (energy resolution = 128 eV) and the INCA software from Oxford Instruments. The aberration-corrected STEM (Hitachi 2700C) was operated at 200 keV, and the corresponding EDXS elemental maps were acquired using a 5030 EDX detector from Bruker. The FESEM images were obtained using the S-4800 (Hitachi Corp.). The cross-sectioned FESEM images and EDXS elemental maps for the 0.4LiI-0.6Li_4SnS_4-coated $LiCoO_2$ electrode were obtained using a JSM-7000F (JEOL) after polishing the cross-sectioned surface at 5 kV for 13 h with an Ar ion beam (JEOL, SM-0910). The weight fraction of the SE coating layer for the 0.4LiI-0.6Li_4SnS_4-coated $LiCoO_2$ powders was determined by inductively coupled plasma optical emission spectroscopy (ICP-OES) using the 720-ES (Varian Corp.). The SE and composite electrode pellets used for characterization were prepared under a pressure of 370 MPa.

Electrochemical Characterization: After the LiI-Li_4SnS_4 pellets were prepared by cold-pressing at 370 MPa, the Li-ion conductivity was measured by an AC impedance method using an Iviumstat (IVIUM Technologies Corp.) with symmetric Li-ion blocking c-Al/SE/c-Al cells, in which the carbon coating layers face the SE. All-solid-state cells were fabricated as follows: Composite electrodes were prepared from the LiI-Li_4SnS_4/$LiCoO_2$ mixture or the LiI-Li_4SnS_4-coated $LiCoO_2$. $Li_{0.5}In$ prepared by mixing In (99%, Sigma-Aldrich) and Li (FMC Lithium Corp.) powders were used as the counter and reference electrode materials. After the SE layer was formed by pelletizing 150 mg of LPS powders by pressing at 74 MPa, 15 mg of the as-prepared composite electrodes was spread, followed by pressing at 370 MPa. Then, 100 mg of the as-prepared $Li_{0.5}In$ was attached on the other side of SE layer by pressing at 370 MPa. All procedures were performed in a polyaryletheretherketone (PEEK) mould (diameter = 1.3 cm) with two Ti metal rods as current collectors. All processes for preparing the SEs and fabricating the all-solid-state cells were performed in an Ar-filled dry box. Galvanostatic charge–discharge cycling test was performed at 30 °C with current densities of 0.11, 0.22, 0.55, 0.77, and 1.10 mA cm^{-2}. The same current density was applied for charge and discharge. The Nyquist plots for the $LiCoO_2$/Li-In cells were obtained after charging at 0.11 mA cm^{-2} (0.1C) to 30 mA h g^{-1} and resting for more than 3 h. The GITT measurements were carried out with a pulse current of 0.55 mA cm^{-2} for 60 s and rest for 2 h. For the dry-air-stability test, 250 mg of LPS or the 0.4LiI-0.6Li_4SnS_4-coated $LiCoO_2$ powders was kept under a flow of dry air (a mixture of O_2 and N_2 with 21/79 vol. ratio).

Supporting Information

Supporting Information is available from the Wiley Online Library or from the author.

Acknowledgements

This work was supported by Basic Science Research Program through the National Research Foundation of Korea (NRF) funded by the Ministry of Education (No. NRF-2014R1A1A2058760), and by the Energy Efficiency & Resources Core Technology Program of the Korea Institute of Energy Technology Evaluation and Planning (KETEP) grant funded by the Korea government Ministry of Trade, Industry & Energy (No. 20152010103470). Experiments at PLS were supported in part by MSIP and POSTECH. This research used the EM facility of the Center for Functional Nanomaterials, which is a U.S. DOE Office of Science Facility, at Brookhaven National Laboratory under Contract No. DE-SC0012704.

Received: October 12, 2015
Revised: November 14, 2015
Published online: December 22, 2015

[1] a) J. B. Goodenough, Y. Kim, *Chem. Mater.* **2010**, *22*, 587; b) M. Armand, J. M. Tarascon, *Nature* **2008**, *451*, 652.
[2] a) K. Xu, *Chem. Rev.* **2004**, *104*, 4303; b) M. Winter, J. O. Besenhard, M. E. Spahr, P. Novák, *Adv. Mater.* **1998**, *10*, 725; c) B. L. Ellis, K. T. Lee, L. F. Nazar, *Chem. Mater.* **2010**, *22*, 691; d) M. Armand, F. Endres, D. R. MacFarlane, H. Ohno, B. Scrosati, *Nat. Mater.* **2009**, *8*, 621; e) A. Manthiram, *J. Phys. Chem. Lett.* **2011**, *2*, 176.
[3] a) N. Kamaya, K. Homma, Y. Yamakawa, M. Hirayama, R. Kanno, M. Yonemura, T. Kamiyama, Y. Kato, S. Hama, K. Kawamoto, A. Mitsui, *Nat. Mater.* **2011**, *10*, 682; b) A. Hayashi, K. Noi, A. Sakuda, M. Tatsumisago, *Nat. Commun.* **2012**, *3*, 856; c) A. Aboulaich, R. Bouchet, G. Delaizir, V. Seznec, L. Tortet, M. Morcrette, P. Rozier, J. M. Tarascon, V. Viallet, *Adv. Energy Mater.* **2011**, *1*, 179; d) N. Ohta, K. Takada, L. Zhang, R. Ma, M. Osada, T. Sasaki, *Adv. Mater.* **2006**, *18*, 2226; e) T. A. Yersak, H. A. Macpherson, S. C. Kim, V. D. Le, C. S. Kang, S. B. Son, Y. H. Kim, J. E. Trevey, K. H. Oh, C. Stoldt, S. H. Lee, *Adv. Energy Mater.* **2013**, *3*, 120; f) Y. Wang, W. D. Richards, S. P. Ong, L. J. Miara, J. C. Kim, Y. Mo, G. Ceder, *Nat. Mater.* **2015**, *14*, 1026; g) Y. S. Jung, D. Y. Oh, Y. J. Nam, K. H. Park, *Israel J. Chem.* **2015**, *55*, 472; h) H. Iba, C. Yada, *17th Int. Meet. Lithium Batteries*, Como, Italy **2014**.
[4] a) F. Mizuno, A. Hayashi, K. Tadanaga, M. Tatsumisago, *Adv. Mater.* **2005**, *17*, 918; b) Y. Seino, T. Ota, K. Takada, A. Hayashi, M. Tatsumisago, *Energy Environ. Sci.* **2014**, *7*, 627.
[5] H.-J. Deiseroth, S.-T. Kong, H. Eckert, J. Vannahme, C. Reiner, T. Zaiss, M. Schlosser, *Angew. Chem. Int. Ed.* **2008**, *47*, 755.
[6] J. Maier, *Nat. Mater.* **2005**, *4*, 805.
[7] a) H. Kitaura, A. Hayashi, K. Tadanaga, M. Tatsumisago, *J. Electrochem. Soc.* **2009**, *156*, A114; b) D. Y. Oh, Y. J. Nam, K. H. Park, S. H. Jung, S.-J. Cho, Y. K. Kim, Y.-G. Lee, S.-Y. Lee, Y. S. Jung, *Adv. Energy Mater.* **2015**, *5*, 1500865.
[8] A. Sakuda, A. Hayashi, M. Tatsumisago, *Sci. Rep.* **2013**, *3*, 2261.
[9] A. Sakuda, A. Hayashi, T. Ohtomo, S. Hama, M. Tatsumisago, *Electrochem. Solid-State Lett.* **2010**, *13*, A73.
[10] Y. J. Nam, S. J. Jo, D. Y. Oh, J. M. Im, S. Y. Kim, J. H. Song, Y. G. Lee, S. Y. Lee, Y. S. Jung, *Nano Lett.* **2015**, *15*, 3317.
[11] Y. Wang, Z. Liu, X. Zhu, Y. Tang, F. Huang, *J. Power Sources* **2013**, *224*, 225.
[12] Z. Liu, W. Fu, E. A. Payzant, X. Yu, Z. Wu, N. J. Dudney, J. Kiggans, K. Hong, A. J. Rondinone, C. Liang, *J. Am. Chem. Soc.* **2013**, *135*, 975.
[13] E. Rangasamy, Z. Liu, M. Gobet, K. Pilar, G. Sahu, W. Zhou, H. Wu, S. Greenbaum, C. Liang, *J. Am. Chem. Soc.* **2015**, *137*, 1384.
[14] S. Teragawa, K. Aso, K. Tadanaga, A. Hayashi, M. Tatsumisago, *J. Power Sources* **2014**, *248*, 939.
[15] S. Yubuchi, S. Teragawa, K. Aso, K. Tadanaga, A. Hayashi, M. Tatsumisago, *J. Power Sources* **2015**, *293*, 941.
[16] T. Kaib, S. Haddadpour, M. Kapitein, P. Bron, C. Schroeder, H. Eckert, B. Roling, S. Dehnen, *Chem. Mater.* **2012**, *24*, 2211.
[17] H. Muramatsu, A. Hayashi, T. Ohtomo, S. Hama, M. Tatsumisago, *Solid State Ionics* **2011**, *182*, 116.
[18] G. Sahu, Z. Lin, J. Li, Z. Liu, N. Dudney, C. Liang, *Energy Environ. Sci.* **2014**, *7*, 1053.
[19] J. R. Hendrickson, P. J. Bray, *J. Magn. Reson.* **1973**, *9*, 341.
[20] a) P. Heitjans, S. Indris, *J. Phys.: Condens. Matter* **2003**, *15*, R1257; b) Y. Deng, C. Eames, J.-N. Chotard, F. Lalere, V. Seznec, S. Emge, O. Pecher, C. P. Grey, C. Masquelier, M. S. Islam, *J. Am. Chem. Soc.* **2015**, *137*, 9136.
[21] P. Bron, S. Johansson, K. Zick, J. S. auf der Guenne, S. Dehnen, B. Roling, *J. Am. Chem. Soc.* **2013**, *135*, 15694.
[22] a) P. G. Bruce, *Solid State Electrochemistry*, Cambridge University Press, New York, USA, **1995**; b) J. Saienga, S. W. Martin, *J. Non-Cryst. Solids* **2008**, *354*, 1475.
[23] J. E. Huheey, E. A. Keiter, R. L. Keiter, *Inorganic Chemistry: Principles of Structure and Reactivity*, 4th ed., HarperCollins College Publishers, New York, USA, **1993**.

[24] R. Kanno, M. Murayama, *J. Electrochem. Soc.* **2001**, *148*, A742.
[25] R. Benedictus, A. Bottger, E. J. Mittemeijer, *Phys. Rev. B* **1996**, *54*, 9109.
[26] Y. S. Jung, K. T. Lee, J. H. Ryu, D. Im, S. M. Oh, *J. Electrochem. Soc.* **2005**, *152*, A1452.
[27] W. Weppner, R. A. Huggins, *J. Electrochem. Soc.* **1977**, *124*, 1569.
[28] a) T. Inada, T. Kobayashi, N. Sonoyama, A. Yamada, S. Kondo, M. Nagao, R. Kanno, *J. Power Sources* **2009**, *194*, 1085; b) S. Ito, S. Fujiki, T. Yamada, Y. Aihara, Y. Park, T. Y. Kim, S.-W. Baek, J.-M. Lee, S. Doo, N. Machida, *J. Power Sources* **2014**, *248*, 943.
[29] J. Zhao, Z. Lu, N. Liu, H.-W. Lee, M. T. McDowell, Y. Cui, *Nat. Commun.* **2014**, *5*, 5088..
[30] J. A. Brant, D. M. Massi, N. A. W. Holzwarth, J. H. MacNeil, A. P. Douvalis, T. Bakas, S. W. Martin, M. D. Gross, J. A. Aitken, *Chem. Mater.* **2015**, *27*, 189.
[31] a) Y. Mo, S. P. Ong, G. Ceder, *Chem. Mater.* **2012**, *24*, 15; b) B. R. Shin, Y. J. Nam, D. Y. Oh, D. H. Kim, J. W. Kim, Y. S. Jung, *Electrochim. Acta* **2014**, *146*, 395; c) F. Han, T. Gao, Y. Zhu, K. J. Gaskell, C. Wang, *Adv. Mater.* **2015**, *27*, 3473.
[32] N. Ohta, K. Takada, I. Sakaguchi, L. Zhang, R. Ma, K. Fukuda, M. Osada, T. Sasaki, *Electrochem. Commun.* **2007**, *9*, 1486.